PHYSICAL REVIEW E **00**, 003000 (2016)

Crack propagation through disordered materials as a depinning transition: A critical test of the theory

Laurent Ponson[1,*] and Nadjime Pindra[1,2]
[1]*Institut Jean le Rond d'Alembert (UMR 7190), CNRS - Université Pierre et Marie Curie, 75005 Paris*
[2]*Département de mathématiques, Université de Lomé, 1515 Lomé, Togo*
(Received 22 May 2016; published xxxxxx)

The dynamics of a planar crack propagating within a brittle disordered material is investigated numerically. The fracture front evolution is described as the depinning of an elastic line in a random field of toughness. The relevance of this approach is critically tested through the comparison of the roughness front properties, the statistics of avalanches, and the local crack velocity distribution with experimental results. Our simulations capture the main features of the fracture front evolution as measured experimentally. However, some experimental observations such as the velocity distribution are not consistent with the behavior of an elastic line close to the depinning transition. This discrepancy suggests the presence of another failure mechanism not included in our model of brittle failure.

DOI: 10.1103/PhysRevE.00.003000

I. INTRODUCTION

Understanding the failure properties of heterogeneous materials has driven a large research effort over last few decades. The motivation is twofold: First, describing the role of material microstructure on the behavior of cracks is a prerequisite to make reliable predictions on the resistance and lifetime of solids. In this respect, this research can find direct application for the design of materials with improved fracture performance [1–3]. Classical concepts of fracture mechanics that describe failure as the propagation of a crack through a homogeneous elastic media miss several aspects of the failure of materials, such as the intermittent dynamics of cracks [4,5] or the scale invariant roughening of fracture surfaces [6–8]. Predicting the overall toughness of a heterogeneous material remains also a challenge. Recently, many progresses were addressed by describing the onset of failure as a depinning transition [9–13]. Here, we thoroughly test this approach through a systematic comparison of the model prediction with experimental data. Second, crack propagation in disordered materials has been shown to exhibit puzzling scaling laws with universal features. As conjectured by Bouchaud *et al.* [6], this suggests that a unified theoretical framework based on critical transition theory may capture the failure properties of a large range of materials with disordered microstructures. It also suggests that fracturing materials could be used as a model system to investigate dynamic phase transition involved in a myriad of other phenomena such as the wetting of liquids on heterogeneous substrates [14], the motion of magnetic domain walls [15], or the dynamics of a dislocation [16] that are dominated by the motion of an interface or a defect line. Proposed in the 1990s [17–19], this connection with this family of critical phenomena has been recently made more quantitative, and various aspects of the intermittent dynamics of cracks [9,20], their scale invariant roughness [21], but also their average dynamics [22,23] could be explained by describing the onset of material failure as a depinning transition. In this theoretical framework, the crack front is described as an elastic line that can propagate through the random arrangement of heterogeneities when the external driving exceeds some critical threshold. The next step along this line of research is to establish a clear separation between properties reminiscent of a depinning transition and nonuniversal features specific to the loading conditions or the material investigated. The identification of the conditions under which criticality does emerge in fracture problems is also an open question.

Motivated by these challenges, we proceed here to a systematic comparison of the predictions of the depinning model with the experimental data available. The goal is to reveal to which extent depinning concepts are relevant to describe the behavior of cracks in disordered materials. We are interested to test the relevance of this approach to capture not only the scaling properties of cracks, but also some other aspects of their complex dynamics by including in the theory the effect of the loading conditions, the geometry of the specimen and the failure properties of the fracturing material. This test of the model will be performed through the comparison of the theory with characteristic features of the dynamics of interfacial cracks recently evidenced by Tallakstad *et al.* in a series of experiments [24]. We will show that the model proposed captures most but not all the statistical properties of the crack front. This discrepancy between theory and experiment will prove to be enlightening, as it will reveal physical ingredients not included in the original model that will be discussed in the final part of the paper.

The focus of our work will be mainly on the dynamics of planar cracks. In materials with a random microstructure, cracks under slow external driving display a jerky dynamics with sudden jumps spanning over a broad range of length scales. Such a complex motion, also referred to as crackling noise [25], is reminiscent of a dynamic phase transition and has been observed in various systems involving the motion of elastic interfaces in media with random impurities, defects or heterogeneities [26,27]. These features have been investigated indirectly in experimental fracturing systems through the acoustic emission accompanying failure [22,28,29], even though a quantitative link between acoustic bursts and sudden crack motions is still missing. More recently, this intermittent dynamic could be studied in great detail using a high-speed and

*laurent.ponson@upmc.fr

high-resolution camera that can track a crack front propagating through a weak heterogeneous plane between two transparent Plexiglas plates [4,30]. As a result, the statistics of the local front velocity could be characterized extensively as a function of the average crack speed [24], and in this work, we intend to compare these statistical features with the model predictions.

Contrary to previous studies that focused only on the scaling properties of cracks [9,31], our approach is designed to also capture nonuniversal features by taking into account the finite distance to the critical point that corresponds to a vanishing crack speed, as in many practical situations, the front moves at slow, however, finite speed. The evolution law for the crack used here is derived rigorously from continuum fracture mechanics [11,32], so it takes into account the loading conditions and the geometry of the fracture test actually used in the experiments. Thus, we expect our approach to capture the value of the exponents involved in the scaling laws, but also more subtle features such as the influence of the average crack growth velocity, the value of the thresholds and constants involved in the scaling laws, or the statistics of local crack growth velocity.

In Sec. II, we describe the model used in our study and the numerical approach for the resolution of the equation of motion of the crack. In Sec. III, we present the predictions of our model and confront them with the experimental observations of Refs. [21,24,30]. The final section, Sec. IV, is a discussion of the success and limitations of the depinning theory for describing material failure and the possible improvements of the current model.

II. MODEL AND METHOD

A. Evolution equation of the crack front

The geometry of the fracture test investigated in this study is inspired by the experiment setup of Refs. [21,24,30] that is presented schematically in Fig. 1(a). An interfacial crack of length $c(z,t)$ propagates between two elastic plates that are separated at a constant opening rate $v_{\text{ext}} = d\delta/dt$. We assume here that all the characteristic length scales of the sample (crack length, plate thickness, etc.) are much larger than both the perturbations along the crack front and the characteristic size of the heterogeneities. Another important assumption is that all the dissipative processes located near the crack tip (for example bond breaking, plasticity, microcracking) are confined in a zone much smaller than the typical heterogeneity size. Then, the problem of planar crack propagation within a three-dimensional (3D) brittle solid can be reduced to a 2D problem where an interface, the crack front, is driven within a plane with heterogeneous fracture properties, as represented schematically in Fig. 1(b) [11,18,32,33]. The equation of motion of the interface can be obtained in three steps [9,11,32]:

(i) The field of driving force along the crack front, i.e., the elastic energy release rate $G(z,t)$, is written as a function of the front configuration $c(z,t)$.

(ii) The material disorder is described through a random field of fracture energy $G_c(x,z)$ that is drawn from a statistical distribution.

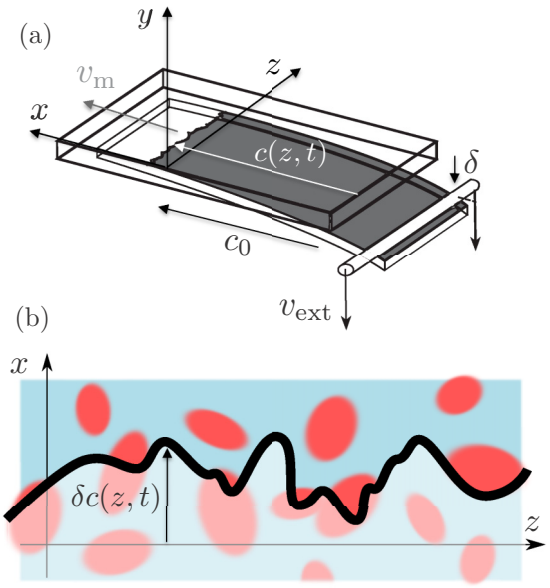

FIG. 1. Geometry of the fracturing system: (a) Sketch of the experimental fracture test where an interfacial crack is made propagate at the weak interface between two elastic plates; (b) Schematic view of the heterogeneous interface where the crack front deforms under the effect of heterogeneities.

(iii) These two previous expressions are used into a kinetic law where the local crack speed increases linearly with the net driving force, $\frac{\partial c}{\partial t} \sim G(z,t) - G_c[z,x = c(z,t)]$.

We now provide the detailed derivation of each of these steps before specializing the derived evolution equation to the fracture experiment investigated in Fig. 1(a).

1. Elastic energy release rate

Material heterogeneities distort the crack line, resulting in a heterogeneous distribution of driving force. To calculate this distribution from the geometrical perturbations of the front, consider first a reference straight configuration $c(z,t) = c_0$ that corresponds to the homogeneous distribution of elastic energy release rate $G(c_0,\delta)$ at the imposed displacement δ. While keeping δ constant, then perturb the crack front within the average crack plane, assuming an infinitely large homogeneous elastic solid under tensile loading conditions. At first order in the front perturbation $\delta c(z) = c(z,t) - c_0$, the elastic energy release rate follows [32]

$$G(z,t) = G(c_0,\delta) + \left.\frac{\partial G}{\partial c}\right|_{c_0,\delta} \delta c(z,t) + \frac{G(c_0,\delta)}{\pi} PV \int_{-\infty}^{+\infty} \frac{\delta c(\tilde{z}) - \delta c(z)}{(\tilde{z}-z)^2} d\tilde{z}, \quad (1)$$

where the principal value (PV) ensures the convergence of the integral. We now take care of the driving imposed to the crack in the experiment of Fig. 1(a). As the displacement δ of the lower plate is increased, the driving $G(c_0,\delta)$ increases too. As a result, the three terms on the right-hand side of Eq. (1) must be updated. However, two of them are already linear in the front perturbation, so we only need to update the first one that is the only one to bring a first-order contribution.

Limiting this analysis to short propagation distance, the opening displacement $\delta = \delta_0 + v_0 t$ can be expressed as the sum of the initial opening with a small variation $v_{\rm ext}\, t \ll \delta_0$ that increases linearly with time where $v_{\rm ext}$ is the opening rate imposed by the test machine [see Fig. 1(a)]. This leads to $G(c_0,\delta) = G(c_0,\delta_0) + \frac{\partial G}{\partial \delta}|_{c_0,\delta_0} v_0 t$ while the two other terms depending on δ in Eq. (1) are replaced by $\partial G/\partial c|_{c_0,\delta_0}$ and $G(c_0,\delta_0)$.

For a stable fracture test geometry, i.e., when the external driving $G(c_0,\delta)$ decreases with the crack length, $\partial G/\partial c|_{c_0,\delta_0}$ is negative. Introducing the structural length $\mathcal{L} = -\frac{G(c_0,\delta_0)}{\partial G/\partial c|_{c_0,\delta_0}}$ and the normalized variations of the driving force

$$g(z,t) = \frac{G(z,t) - G(c_0,\delta_0)}{G(c_0,\delta_0)}, \tag{2}$$

Eq. (1) can be rewritten as

$$g(z,t) = \frac{v_{\rm m} t - \delta c(z,t)}{\mathcal{L}} + \frac{PV}{\pi}\int_{-\infty}^{+\infty} \frac{\delta c(\tilde{z},t) - \delta c(z,t)}{(\tilde{z}-z)^2} d\tilde{z}. \tag{3}$$

We have introduced here the velocity $v_{\rm m} = -\frac{\partial G/\partial \delta|_{c_0,\delta_0}}{\partial G/\partial c|_{c_0,\delta_0}} v_{\rm ext}$ imposed by the loading machine to the crack. For the fracture test of Fig. 1(a), the unperturbed driving force follows $G(\delta,c) = \frac{Eh^3\delta^2}{3c^4}$ [34] where E is the Young's modulus of the material and h the lower plate's thickness. This leads to $\mathcal{L} = c_0/4$ and $v_{\rm m} = c_0/(2\delta_0)\, v_{\rm ext}$.

Equation (3) calls for a few comments. The constant opening rate imposed to the fracturing specimen considered in Fig. 1 turns out to be equivalent to pull on the crack line with an array of springs of effective stiffness $1/\mathcal{L}$ driven at the velocity v_m. Thus, this amounts to consider that the crack line is trapped in a potential well moving at some constant velocity, as classically considered in disorder elastic interface problems [35,36]. The nonlocal term in (3) describes the interactions along the front. This effective line elasticity will compete with the effect of the disorder, as it tends to straighten the crack front.

2. Fracture energy

We now turn to the description of the material fracture properties in our model. We start by reminding the experimental procedure followed for preparing the specimen shown in Fig. 1(a). Before sintering both Plexiglas plates together through a heat treatment, one of the surface is sandblasted so that the interface is heterogeneously consolidated. This introduces variations in the fracture properties that we describe through a spatially varying field of fracture energy $G_c(x,y)$. We then assume that this field is characterized by a correlation length ξ that corresponds to the typical heterogeneity size possibly related to the bead diameter used for the sandblasting [21]. The strength of each heterogeneity is subsequently drawn in a Gaussian distribution of average value $\langle G_{\rm c}\rangle$ and standard deviation $\delta G_{\rm c}$, and introduce the normalized variations of the toughness field

$$g_{\rm c}(z,x) = \frac{G_{\rm c}(z,x) - \langle G_{\rm c}\rangle}{\langle G_{\rm c}\rangle}. \tag{4}$$

In the remainder of the study, we keep $\sigma = \frac{\delta G_{\rm c}}{\langle G_{\rm c}\rangle}$, the relative fracture energy fluctuations, equal to one. This ensures that the front is within the so-called strong pinning regime and that its evolution gives rise to an intermittent dynamics that is the main focus of this work. With this parameter value, the Larkin length $L_{\rm Larkin} \simeq \xi/\sigma^2$ [13,37,38], that gives the extent of the smallest avalanches, is of the same order than the heterogeneity size ξ that is also the smallest physical length scale in our model. Note that an estimation of the experimental value $\sigma^{\rm exp}$ is possible from the geometry of the crack line. Indeed, its height-height correlation function is expected to follow $\delta_z f(\delta z) \simeq c\,\sigma^{2\zeta}\xi^{1-\zeta}\delta z^{\zeta}$ [13], leading to $\delta_z f(\xi)/\xi \simeq c\,\sigma^{2\zeta}$ where $\zeta^{\rm th} \simeq 0.39$ is the roughness exponent and c is a constant that can be measured numerically (see Sec. III A). The experiments of Santucci *et al.* [21] provide a satisfactory agreement with this prediction. First, the experimental roughness exponent $\zeta^{\rm exp} \simeq 0.35$ is close to the theoretical value. Second, the roughness $\delta_z h(\xi)$ computed in $\delta z = \xi$ scales linearly with ξ when the characteristic size ξ of the disorder is approximated by the lower bound of the self-affine regime. These observations reinforce the following estimation $\sigma^{\rm exp} \simeq [\delta_z h(\xi)/c\,\xi]^{1/2\zeta} \simeq 0.4$, where the disorder strength seems to be constant while its characteristic size were varied using beads of different diameters for sandblasting the interface. This value is smaller than the one chosen in the simulations, however, sufficiently close to unity to allow a proper comparison between simulations and experiments as both are in the strong pinning regime.

3. Kinetic crack growth law

To predict the evolution of the crack, its local speed is generally assumed to vary linearly with the local net driving force $v \sim G - G_{\rm c}$ [9,33,39,40]. Here, we justify this linear kinetic law from Griffith's equilibrium condition $G = G_{\rm c}(v)$ where the dependance of the fracture energy with the crack speed v is taken into account [41,42]. Indeed, the linearization of the fracture energy $G_{\rm c}(v) = G_{\rm c}(v_{\rm m}) + dG_{\rm c}/dv|_{v_{\rm m}}(v - v_{\rm m})$ around the average crack speed gives

$$\frac{v - v_{\rm m}}{v_0} = \frac{G - G_{\rm c}(v_{\rm m})}{G_{\rm c}(v_{\rm m})}, \tag{5}$$

where the characteristic velocity $v_0 = \frac{G_c(v_{\rm m})}{dG_{\rm c}/dv|_{v_{\rm m}}}$ follows from the fracture properties of the interface. This equation of motion has recently been shown to capture successfully the relaxation dynamics of a crack depinning from a single obstacle [43]. On a general manner, v_0 varies with the crack speed $v_{\rm m}$. Interestingly, a fit of the experimental data of Ref. [44] with the law $G_{\rm c} \sim (1 + v/v_{\rm c})^{\gamma}$, gives a rather constant value $v_0 \simeq 140\ \mu{\rm m.s}^{-1}$ over the investigated range of crack speeds $0.4\ \mu{\rm m.s}^{-1} \leqslant v_{\rm m} \leqslant 40\ \mu{\rm m.s}^{-1}$ for the fitted parameters $v_{\rm c} \simeq 5\ \mu{\rm m.s}^{-1}$ and $\gamma \simeq 0.07$.

4. Evolution equation

The derivation of an evolution equation for the crack is now in order, as it suffices to insert the expressions (3) and (4) of the elastic energy release rate and the fracture energy into the kinetic law of Eq. (5). Considering small enough crack perturbations $\delta c \ll c_0$, one can decouple the zeroth-order equation $G(c_0,\delta_0) = \langle G_{\rm c}(v_{\rm m})\rangle$ from the first-order one $\frac{\partial \delta c/\partial t - v_{\rm m}}{v_0} = g(z,t) - g_{\rm c}[z, x = \delta c(z,t)]$. After normalization of this equation using the dimensionless quantities

$f(z,t) = \delta c(z,t)/\mathcal{L}$, $u = z/\mathcal{L}$, $w = x/\mathcal{L}$ and $\tau = v_0/\mathcal{L} \times t + 1$, one obtains

$$\frac{\partial f}{\partial \tau} = \frac{v_m}{v_0}\tau - f + \frac{PV}{\pi}\int_{-\infty}^{+\infty} \frac{f(\tilde{u}) - f(u)}{(\tilde{u}-u)^2} d\tilde{u} - \eta_c(u,f). \tag{6}$$

This expression reveals that three independent parameters only govern the crack front dynamics: the correlation length $\xi/\mathcal{L}$ of the random quenched noise $\eta_c(u,w) = g_c(\mathcal{L}u, \mathcal{L}w)$, the disorder strength $\sigma = \langle\sqrt{\eta_c(u,w)^2}\rangle_{u,w}^{1/2} = \langle\sqrt{g_c(z,x)^2}\rangle_{z,x}^{1/2}$ and the driving parameter v_m/v_0.

This evolution equation provides a powerful tool to make predictions on the dynamics of crack fronts that will be subsequently compared with experiments. Let us note that a similar equation is involved in various physical situations where an interface is driven in a medium with random defects or impurities, and is known to give rise to the so-called depinning transition: under force-controlled loading conditions, the front is pinned by the disorder and remains stable up to some critical value G_c^{ext} of the applied driving force. As in classical critical transitions, the order parameter, the macroscopic velocity of the interface, is then expected to increase as a power law $v_m \sim (G^{ext} - G_c^{ext})^\theta$ of the distance to the critical point, i.e., the difference between the applied force G^{ext} and the critical one G_p^{ext}, with an exponent $\theta^{th} \simeq 0.625 \pm 0.005$ [45–49]. In addition, power-law-distributed fluctuations are expected to emerge from the front behavior, involving length and time scales that diverge at the depinning threshold. In crack propagation problems, many of these features were evidenced in experiments and shown to compare qualitatively, and to some extent quantitatively, with the predictions derived using the concept of depinning transition [50,51].

However, in most experimental situations such as the one represented in Fig. 1, fracture is achieved under displacement controlled conditions. The force applied to the interface may then fluctuate during propagation and can be inferred from the elongation of the effective springs that drive the interface using $G^{ext}(t) = \langle G_c(v_m)\rangle(1 + \frac{v_m t - \langle \delta c(z,t)\rangle_z}{\mathcal{L}})$. It can be shown that as the driving velocity v_m goes to zero, the net applied force G^{ext} tends toward its critical value G_c^{ext}. In other words, under displacement-controlled conditions, the driving velocity plays the role of the control parameter and defines the distance to the critical point. In the evolution equation (6), it is controlled by the driving parameter v_m/v_0. As studying different distances to the critical point is an efficient way to characterize the depinning transition, we will investigate various crack speeds following the experimental procedure of Tallakstad *et al.* [24]. However, as the focus is on the local fluctuations in the crack evolution and not on the global avalanches, we could not evidence significant change in the crack behavior, similarly to the experimental observations [24]. To circumvent this difficulty, we will then use the concept of waiting time matrix introduced by Mäløy *et al.* [7] that, once thresholded at different time scales, reveals velocity fluctuations corresponding to different distances to the depinning threshold. In other words, we will show how scaling behaviors characterizing the evolution of the system towards criticality can be extracted from the system dynamics at some fixed and finite distance to the critical point.

The dimensionless stiffness $\xi/\mathcal{L}$ of the spring driving the crack line also controls the distance to the critical point. Barès *et al.* showed a transition from a continuum to a crack-line-like dynamics as this parameter is significantly decreased. Here, we choose a small parameter value $\xi/\mathcal{L} = 4\xi/c_0 = 10^{-3}$ of the same order than the experimental one that ensures a critical behavior of the crack line.

Since the evolution equation (6) is strongly nonlinear due to the presence of the front perturbation f as an argument of the disorder term η_c, predicting analytically the detailed statistical properties of the crack dynamics remains a very challenging task [see for example Ref. [52] for a review of the appropriate analytical methods based on the functional renormalization group (FRG) theory]. In addition, analytical treatments provide only approximated solutions, strictly valid at the critical dimension d_c, where d is the interface dimension with $d_c = 2$ and $d = 1$ for crack propagation problems. As a result, we choose to solve the evolution equation (6) numerically following the procedure described in the next section, and to compare our results with the FRG predictions and other numerical findings when possible.

B. Numerical resolution of the evolution equation

To predict the crack line dynamics, we focus on the dimensionless evolution equation (6) and follow the numerical procedure used by Bonamy *et al.* [9]. The crack front position is discretized over N_z points with position $u_i = u_i/\mathcal{L} = L_z/\mathcal{L} \times i/N_z$ for $1 \leqslant i \leqslant N_z$ where $L_z = N_z \times \xi$ is the front length along the z axis. As a result, at a given time τ, the front configuration is described by the N_z values $\{f_1(\tau), f_2(\tau), \ldots, f_{N_z}(\tau)\}$. We impose periodic boundary conditions along the z axis, so that a front of $2N_z$ points with $f_{bc} = \{f_{N_z/2+1}, \ldots, f_{N_z}, f_1, \ldots, f_{N_z}, f_1, \ldots, f_{N_z/2}\}$ is actually considered for the sake of the numerical calculation. Using this discretization, the evolution equation leads to N_z linear equations:

$$f_i(\tau + \delta\tau) = f_i(\tau) + \delta\tau \times \{\mathcal{G}_i[f_1(\tau)\ldots f_{N_z}(\tau)] - \eta_c[u_i, f_i(\tau)]\} \tag{7}$$

with $1 \leqslant i \leqslant N_z$ where the unknown are the $f_{1\leqslant i\leqslant N_z}$'s and the driving force is given by $\mathcal{G}_i = \frac{v_m}{v_0}\tau - f_i(\tau) + \frac{PV}{\pi}\int_{f_i(\tau)-L_z/\mathcal{L}}^{f_i(\tau)+L_z/\mathcal{L}} \frac{f_{bc}(\tilde{u},\tau) - f_i(\tau)}{(\tilde{u}-u_i)^2} d\tilde{u}$. This explicit scheme allows for the rapid calculation of the front position at time $\tau + \delta\tau$ from its position at time τ, so that large systems of size $N_z = 5000$ could be investigated.

The disordered field $\eta_c(u_i, w_i)$ that describes the local resistance to failure is discretized on a square grid $(1 : N_z) \times (1 : N_z)$ where the elementary steps are of size $\xi/\mathcal{L}$. The value of η_c in each node is drawn from a Gaussian distribution with unit standard deviation and zero mean value. The value of the toughness at the actual location of the front $\{u_i, w_i = f(u_i,\tau)\}$ is extrapolated from the toughness value of the two neighboring nodes of same abscissa u_i. The physical discretization step along the front direction is kept equal to the heterogeneity size ξ. This choice is motivated by our interest in the properties of the front at scales larger than the disorder correlation length ξ. At smaller scales, the front dynamics might be governed by failure processes such as microcracking

that are not taken into account in our model. The effect of such a damage percolation process on the crack dynamics has recently been studied through an alternative computational fracture model [53] and the comparison of their results with our predictions will be used in the discussion section to interpret the experimental observations.

The crack evolution is calculated incrementally by starting from a straight crack front at time $\tau = 0$ and then computing $f(\tau + \delta\tau)$ from the geometry $f(\tau)$ of the front at time τ using Eq. (7). We can then come back to the quantities of interest in physical units such as the crack length δc or the time t by multiplication by the normalization constants ξ and $\mathcal{L}/v_0$. The front position is calculated over a large number of time steps, typically 10^6, which corresponds to a propagation distance $L_x = N_x\,\xi$ of about $N_x = 100\,\xi$ heterogeneity sizes. This distance is several times larger than the one crossed by the crack during the experiments of Tallakstad *et al.* [24], as we want to ensure an accurate determination of the crack statistical features through a large sampling. However, the propagation distance $\delta c(z,\tau+\delta\tau) - \delta c(z,\tau) \ll \xi$ between each time step remains small for any position z, ensuring the convergence of our numerical scheme. For the postanalysis, only 10% of the computed profiles are kept. This corresponds to about $N_t \simeq 10\,000$ crack positions that are separated by the time step $\Delta\tau$. $\Delta\tau$ is small enough to ensure that the front spent at least one time step on each pixel of the grid. This choice takes inspiration from the experimental procedure where the acquisition rate of the camera is set so that the waiting time matrix that counts the time spent by the front in every pixel does not contain any zeros. Finally, the transient regime where the front geometry keeps memory of the initial straight condition is systematically removed for the post-treatment. This zone extends over a few tenths of heterogeneity size in the propagation direction.

For each numerical simulation, we extract three quantities that will be used later for the statistical characterization of the front dynamics.

(i) The spatiotemporal evolution of the front is stored in the matrix $[f_i(\tau_j)]_{1\leqslant i\leqslant N_z, 1\leqslant j\leqslant N_t}$.

(ii) The local velocity of the crack front is stored in the matrix $(v_{i,j}^{\text{front}})_{1\leqslant i\leqslant N_z, 1\leqslant j\leqslant N_t-1}$ where $v_{i,j}^{\text{front}} = v_0 \frac{f_i(\tau_j+\Delta\tau)-f_i(\tau_j)}{\Delta\tau}$. The driving velocity sets the average front velocity $\langle v_{i,j}^{\text{front}}\rangle_{i,j} = v_m$.

(iii) The time spent by the front in each pixel $(z_i,\ x_i)$ of the grid is stored in the so-called waiting time matrix $(w_{i,j})_{1\leqslant i\leqslant N_z, 1\leqslant j\leqslant N_x}$. This quantity has been introduced in Ref. [30] to characterize the avalanche dynamics of the crack front. From it, we define the velocity matrix $(v_{i,j})_{1\leqslant i\leqslant N_z, 1\leqslant j\leqslant N_x}$ where $v_{i,j} = 1/w_{i,j}$. This quantity is different from the front velocity $v_{i,j}^{\text{front}}$ introduced previously, even though a relationship can be established between their probability density function [24].

Following the experimental procedure, we performed simulations at four different imposed velocities ranging in $5\times10^{-4} \leqslant v_m/v_0 \leqslant 2.5\times10^{-2}$. The relevant parameters corresponding to each velocity are listed in Table I. This range corresponds about to the smallest crack speeds investigated by Tallakstad *et al.* [24], as the experimental range is $2\times10^{-4} \lesssim v_m/v_0 \lesssim 1$ where the characteristic velocity $v_0 \simeq 140\,\mu\text{m.s}^{-1}$ has been estimated in Sec. II A 3. In particular, it includes the specific experiment used to investigate the local avalanche statistics that corresponds to $v_m \simeq 1\times10^{-2}\,v_0$ [24] and that we will use in the following.

TABLE I. Numerical parameters and loading conditions used for each simulation: imposed driving velocity v_m normalized by the characteristic velocity introduced in Sec. II A 3, time step $\Delta\tau$ between two successive recorded front positions, average distance Δx crossed during the time step $\Delta\tau$, total number N_t of recorded profiles, and distance L_x crossed during the whole simulation expressed in heterogeneity size ξ. For all the simulations, the structural length $\mathcal{L} = 1000\,\xi$ and the disorder strength $\sigma = 1$ are kept the same.

v_m/v_0	$\Delta\tau$	$\Delta x/\xi$	N_t	L_x/ξ
5.0×10^{-4}	1.0×10^{-2}	5×10^{-3}	20 000	100
2.5×10^{-3}	3.2×10^{-3}	8×10^{-3}	10 000	80
5.0×10^{-3}	1.6×10^{-3}	8×10^{-3}	10 000	80
2.5×10^{-2}	3.2×10^{-4}	8×10^{-3}	10 000	80

III. STATISTICAL CHARACTERIZATION OF THE CRACK EVOLUTION

In this section, we compare the statistical properties of the crack front predicted by the depinning model with the experimental observations. We first study the geometrical properties of the crack front through the scaling properties of its roughness. Then, we move to the dynamical properties and investigate the correlations between local front velocities, the size distribution of local avalanches and finally the crack speed distribution.

A. Height correlations

Spatial variations of the local resistance result in geometrical perturbations of the crack front that we study here. The computed crack evolution provides the dimensionless front fluctuations $\delta f(u,\tau) = f(u,\tau) - v_m/v_0\,\tau$ with respect to the mean drift, and hence the physical fluctuations $\delta c(z,t) = f(z,t) - v_m\,t$, from which we compute the autocorrelation functions

$$\begin{aligned}\Delta_z f(\delta z) &= \langle[\delta c(z+\delta z,t) - \delta c(z,t)]^2\rangle_{z,t}^{1/2}\\ \Delta_x f(\delta x) &= \langle[\delta c(z,t+\delta x/v_m) - \delta c(z,t)]^2\rangle_{z,t}^{1/2}\end{aligned} \tag{8}$$

These correlations are investigated in Fig. 2 along the crack front and the propagation direction. We observe power-law behaviors

$$\begin{aligned}\Delta_z f(\delta z) &\propto \delta z^{\zeta}\\ \Delta_x f(\delta x) &\propto \delta x^{\beta}\end{aligned} \tag{9}$$

with exponents $\zeta = 0.38 \pm 0.02$ and $\beta = 0.45 \pm 0.05$. This result is consistent with the theoretical and numerical predictions for an elastic line with long-range elasticity driven in a disordered medium both for the roughness exponent $\zeta^{\text{th}} \simeq 0.388$ [18,54–57] and the so-called growth exponent $\beta^{\text{th}} \simeq 0.495$ [49,54,55]. The value of the roughness exponent is also consistent with the experimental value $\zeta^{\text{exp}} \simeq 0.35 \pm 0.05$

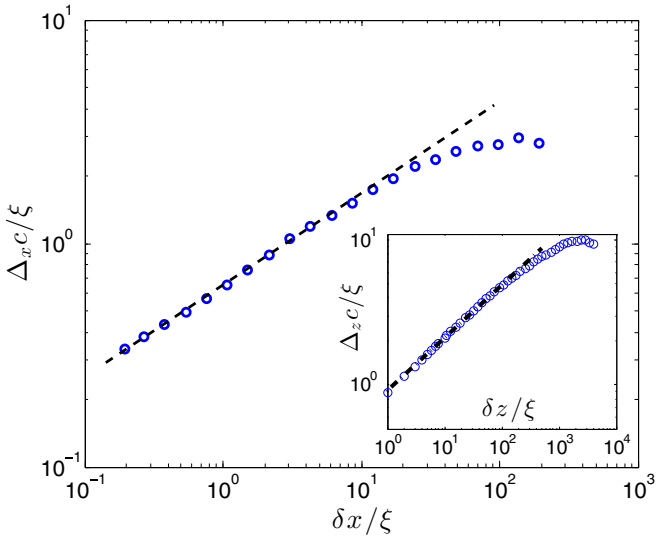

FIG. 2. Correlation functions of the geometrical perturbations of the crack front for the driving velocity $v_m = 5.0 \times 10^{-4}\, v_0$. We observe a self-affine behavior both along the crack front direction (in inset) and the propagation direction (main panel) with exponents $\zeta \simeq 0.38 \pm 0.02$ and $\beta \simeq 0.45 \pm 0.05$, respectively.

measured at large scales from images of the crack front as it propagates between the two Plexiglas plates [21].

The growth exponent, classically measured from the transient roughening of the interface from an initial straight front condition [58], can also be measured in the stationary regime by computing the autocorrelation function of Eq. (8) in the propagation direction [8,59]. In our simulations, we use the smallest driving velocity $v_m = 5 \times 10^{-4}\, v_0$ that turned out to give a reliable measurement $\beta \simeq 0.45$. It is found to take a larger value than the roughness exponent, in agreement with the theoretical predictions of depinning model and the experimental values $\beta^{\text{exp}} \simeq 0.5 - 0.55$ [4,24].

B. Velocity correlations

In the strong pinning regime, the motion of the crack is characterized by an alternation of stick periods during which the front is at rest with slip periods called avalanches corresponding to the rapid advance of some regions of the front [4,9,31]. The spatial structure of a typical avalanche as obtained in the crack growth simulation of Laurson *et al.* [31] is shown in Fig. 3. A striking feature is that the region crossed by the crack during an avalanche is not compact, but instead composed of several clusters. This complex morphology results from the long-range elasticity of the crack line described by the integral term in the expression (1) of the elastic energy release rate: an advance of the crack somewhere along the front results in a redistribution of the driving force in an extended region. This may trigger the detachment of some parts of the crack line that are not in the close vicinity of the initiation zone of the avalanche.

The correlations between the local crack speed at different times may provide insights on this process, as we expect velocities corresponding to the same avalanche to be correlated. As a result, we seek in this paragraph to characterize the

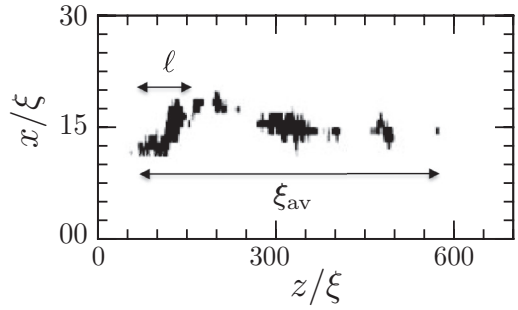

FIG. 3. Spatial structure of a typical avalanche as observed during the simulation of the propagation of a crack in a disordered material for a vanishing front velocity $v_m \to 0$ (courtesy of Laurson *et al.* [31]). ξ_{av} and ℓ represent the lateral size along z of the avalanche and its largest cluster, respectively. Their corresponding depth along the propagation direction are noted $\xi_{\text{av,x}}$ and ℓ_{x}.

temporal correlation of the velocity fluctuations defined as $\delta v^{\text{front}}(z,t) = v^{\text{front}}(z,t) - v_m$ that we compare subsequently with the experimental observations. Our approach consists in exploring how the velocity fluctuation at time t correlates with the velocity fluctuation at time $t + \delta t$ for a fixed position z along the front. The correlation function

$$C(\delta t) = \frac{\langle \delta v^{\text{front}}(z,t+\delta t) \times \delta v^{\text{front}}(z,t) \rangle_{z,t}}{\langle \delta v^{\text{front}}(z,t)^2 \rangle_{z,t}} \qquad (10)$$

is thus computed for the four velocities v_m investigated and represented in Fig. 4. They all show an exponential decay with a characteristic time $\delta t^\star$ that decrease with v_m, as shown in inset. We observe in fact that $\delta t^\star$ is inversely proportional to v_m, and hence

$$C(\delta t) \simeq e^{-\delta t/\delta t^*} \quad \text{with} \quad \delta t^\star \simeq \frac{l_0}{v_m}, \qquad (11)$$

where $l_0 \approx 0.2\,\xi$. This behavior is in excellent agreement with the experimental observations of Ref. [24] where a similar

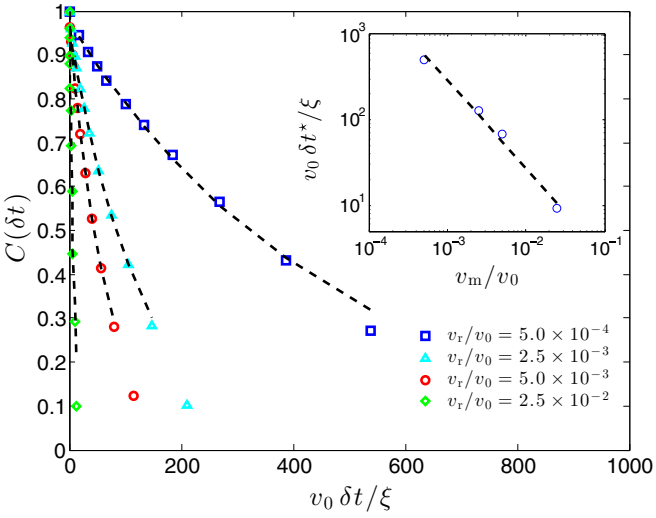

FIG. 4. Correlations between the velocity fluctuations at time t and at time $t + \delta t$ for a fixed position z along the front, as defined in Eq. (10). It shows an exponential decay over a characteristic time $\delta^\star$ that is represented in inset as a function of the driving velocity v_m.

variation of the velocity correlation function with $l_0 \approx 0.1 \times \xi$ were reported.

3 How do we interpret this remarkable property? As reminded in Sec. II A 4, the driving velocity controls the distance to the critical point in the depinning transition. Therefore, as v_m decreases, the size and duration of the largest avalanches increase, and in particular their depth $\xi_{av,x}$. To relate $\xi_{av,x}$ to v_m, we predict first the scaling of the avalanche lateral extent $\xi_{av} \sim v_m^{-\nu/\theta}$ using the definition of the velocity exponent θ reminded in Sec. II A 4 and the correlation length exponent ν that describes the divergence $\xi_{av} = (G^{exp} - G_c^{ext})^{-\nu}$ of the avalanche size close to the depinning threshold. The avalanche depth $\xi_{av,x} \sim \xi_{av}^{\zeta} \sim v_m^{-\zeta\,\nu/\theta}$ then follows using the roughness exponent ζ that characterizes not only the crack roughness (see Sec. III A), but also the aspect ratio of avalanches [58]. We can then determine the time $\delta t^\star = \xi_{av,x}/v_0 \sim v_m^{-\zeta\,\nu/\theta}$ required to the front to cross the largest cluster that corresponds to the correlation time of the velocity fluctuations. The predicted exponent takes the simplified form $\zeta\,\nu/\theta = \beta/(1-\beta)$ after using the scaling relation $\theta = \nu(z-\zeta)$ [60] that involves the dynamic exponent $z = \zeta/\beta$. It takes a value $\beta^{th}/(1-\beta^{th}) \simeq 0.98 \pm 0.02$ close to unity using the numerically determined value of the growth exponent $\beta^{th} \simeq 0.495 \pm 0.005$ [49].

Two important assumptions have been made here. First, the depth of the largest cluster has been approximated by the depth of the total avalanche. According to the numerical observation of Fig. 3, this looks like a fair assumption that relies on the anisotropic spatial structure of the avalanches that extend along the front direction rather than along the propagation direction. Second, we have assumed that the velocity during the propagation of the crack over one cluster is set by the velocity v_0, as observed during the depinning from a single obstacle [43]. This must not be confused with the typical crack velocity $\xi_{av,x}/\xi^z \sim v_m$ during the whole avalanche that scales linearly with the average speed.

This last observation has an interesting consequence, as the macroscopic distance crossed by the crack over the characteristic time scale $\delta t^\star$ follows $\delta x^\star = v_m\,\delta t^\star \simeq l_0$ that is very small compared to the heterogeneity size ξ [see Eq. (11)]. This implies that the local front velocities along the propagation direction are essentially uncorrelated if one investigate two successive positions separated of at least $\delta x^\star \simeq l_0 \ll \xi$. As noticed by Tallakstad *et al.* [24], this implies that the height fluctuations of the front along the propagation direction follow a random walk with exponent $\beta = 1/2$. This provides a simple interpretation of the numerically determined value of the growth exponent $\beta \simeq 0.495 \pm 0.005$ [49]. Note that this property is specific to long-range elasticity. For example, the short-range depinning model exhibits a divergence of the characteristic distance $\delta x^\star$ in the limit of small driving velocity, and so a nontrivial value of the growth exponent $\beta \simeq 0.83$ [61].

To summarize, the divergence of the characteristic time $\delta t^\star \sim 1/v_m$ emerging from the velocity fluctuations in our simulations and in the experiments of Tallakstad *et al.* [24] is signature that the crack is brought closer to the critical depinning transition as the driving velocity vanishes.

C. Statistics of pinning and depinning clusters

We now go further in the characterization of the avalanche dynamics of the fracture front by exploring the size distribution of the depinning clusters shown in Fig. 3. Inspired by Tallakstad *et al.* [24], we also study the size distribution of pinning clusters that reflect the pinned configurations of the front during the stick phases. To study both type of clusters, we apply the procedure proposed by Mäløy *et al.* [30]: We start from the waiting time matrix defined in Sec. II B that provides the time spent by the crack front on each pixel of the grid. The inversion of each individual element of this matrix gives the so-called velocity matrix V that is then thresholded following the procedure

(i) depinning regime

$$V_d^{thres} = \begin{cases} 1 & \text{if } v_{i,j} \geqslant C\,v_m \\ 0 & \text{if } v_{i,j} < C\,v_m \end{cases};$$

(ii) pinning regime

$$V_p^{thres} = \begin{cases} 1 & \text{if } v_{i,j} \leqslant v_m/C \\ 0 & \text{if } v_{i,j} > v_m/C \end{cases}.$$

This procedure reveals both pinning and depinning clusters. Typical thresholded velocity matrices corresponding to $v_m = 5 \times 10^{-4} v_0$ are represented in Fig. 5 in both regimes. The white regions, representing about 35% of the total area, correspond to unity while black ones correspond to zero. These maps ave

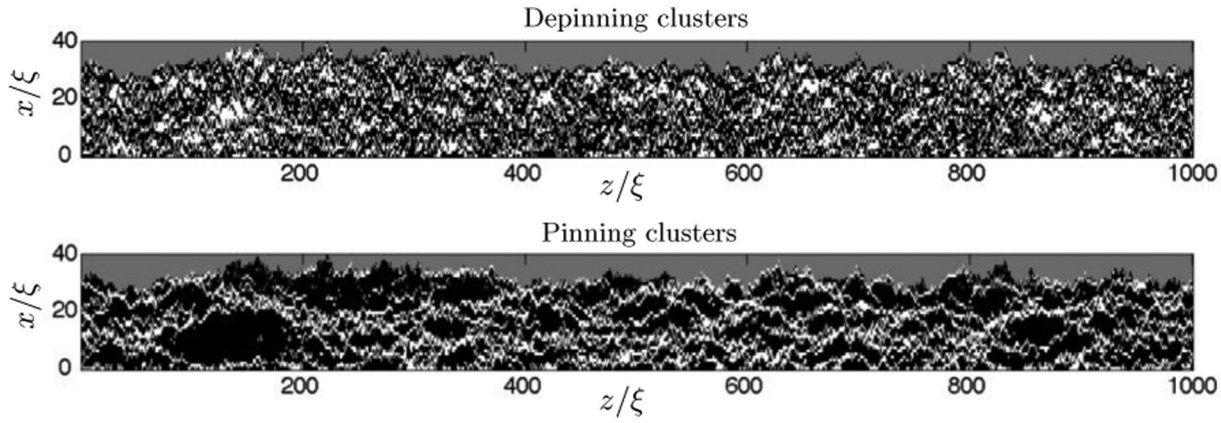

FIG. 5. Representation of the threshold velocity matrices V_d^{thres} and V_p^{thres}. For the depinning case, relatively large areas represented in white correspond to rapid advances of the front, while for the pinning case, the rather thin lines corresponds to front position at arrest for some time.

been obtained using a threshold value $C = 0.6$ for depinning and $C = 10$ for pinning. Note that both figures correspond to the same fractured area of $40\,\xi \times 1000\,\xi$ that represents only a portion of the total domain $100\,\xi \times 5000\,\xi$ actually computed and used for the following postanalysis. These cluster maps look qualitatively similar to the experimental ones shown in Fig. 9 of Ref. [24]. Note however two important differences: The computed maps are about ten times larger than the experiment ones after normalizing the distances by the heterogeneity size ξ. Note also that the spatial resolution of the experimental maps is about ten times smaller than ξ, while the computed map is resolved until ξ. This may explain why the depinning clusters look somehow bigger in the experiments. We now proceed to a quantitative comparison between the experimental and computed cluster maps.

We focus in the following on the slowest driving velocity $v_m = 5 \times 10^{-4} v_0$. The depinning clusters are defined from the depinning cluster map from the domains of connected pixels for which the local velocity is greater than the threshold $C v_m$. They can be clearly identified on the depinning threshold velocity matrix of Fig. 5. Similarly, the pinning clusters are defined from the domains of connected pixels for which the local velocity is lower than the threshold v_m/C. Each of these clusters is characterized by several quantities: their width ℓ_z along the crack front direction, their depth ℓ_x along the propagation direction and their size S corresponding to the total area of the cluster. The statistical distribution of these quantities is now used to quantify the intermittent crack dynamics and compare the simulation results with the experiments.

Figure 6 shows the size distribution of pinning and depinning clusters for different values of the threshold C. We describe their variations with a power law with an exponential cutoff

$$\begin{aligned} P(S_d) &\sim S_d^{\gamma_d} e^{-S_d/S_d^\star} \quad \text{with} \quad S_d^\star \sim C^{-\sigma_d} \\ P(S_p) &\sim S_p^{\gamma_p} e^{-S_p/S_p^\star} \quad \text{with} \quad S_p^\star \sim C^{-\sigma_p} \end{aligned} \tag{12}$$

in both regimes and determine the values of the exponents γ and σ by optimizing the collapse of distributions with different C values on a same master curve. This procedure gives the exponents $\gamma_d = 1.55 \pm 0.05$ for the depinning clusters and $\gamma_p = 1.65 \pm 0.10$ for the pinning clusters. The behavior of Eq. (12) and the value of these exponents are compatible with the experiments where $\gamma_d^{\text{exp}} \simeq \gamma_p^{\text{exp}} \simeq 1.56 \pm 0.04$ were measured [24]. It is also consistent with the results of Laurson *et al.* [31] who measured $\gamma_d = 1.53 \pm 0.05$ through an independent numerical approach. Finally, it is compatible with the theoretical prediction $\gamma_d^{\text{th}} \simeq 1.56$ obtained from the scaling relation $\gamma_d^{\text{th}} = 2\tau - 1$ [31] using the global avalanche exponent $\tau^{\text{th}} = 2 - 1/(1 - \zeta^{\text{th}}) \simeq 1.28$ [35,62].

Interestingly, the exponents $\sigma_d = 3.8 \pm 0.2$ and $\sigma_p = 1.3 \pm 0.1$ predicted by our simulations that characterize the variations of the cut-off sizes $S_d^\star$ and $S_p^\star$ with the threshold C do not match the experimental values $\sigma_d = 1.77 \pm 0.16$ and $\sigma_p^{\text{exp}} = 2.81 \pm 0.23$.

To confirm this discrepancy, we propose to determine the predicted values of σ_d and σ_p through an independent method that will also shed light on their physical significance. We follow the idea of Ref. [24], and compute in Fig. 7 the number

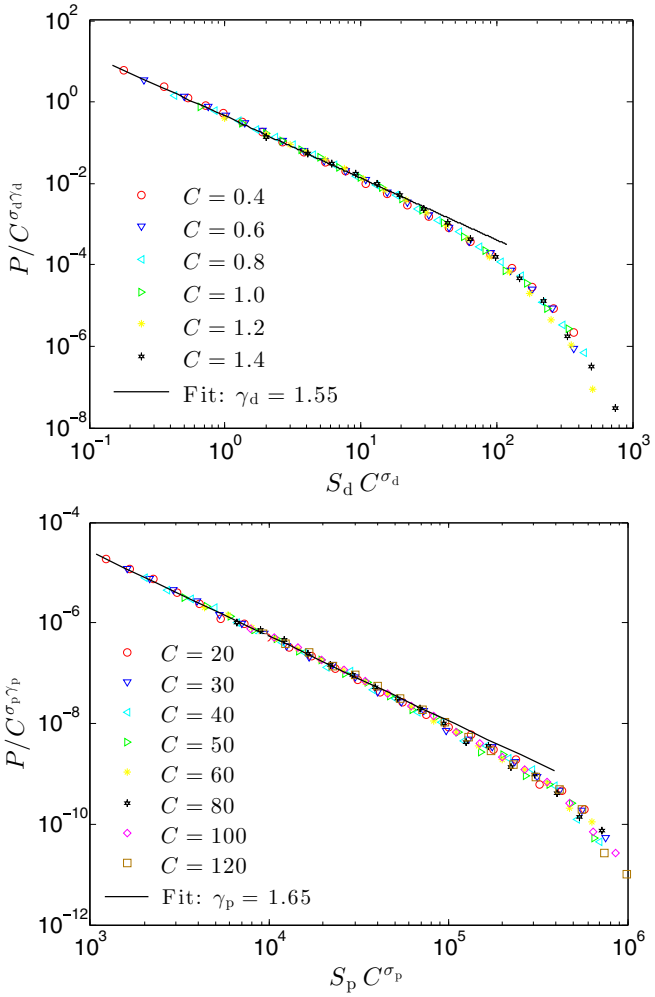

FIG. 6. Normalized distributions of sizes of depinning clusters (top) and pinning clusters (bottom) for various values of the threshold C. Both families of distributions are well described by the power law behavior of Eq. (12) with exponents $\gamma_d = 1.55 \pm 0.05$ and $\gamma_p = 1.65 \pm 0.10$ that are compatible with the experimental findings [24]. On the contrary, the scaling of the cutoffs $S_d^* \sim C^{-\sigma_d}$ and $S_p^* \sim C^{-\sigma_p}$ lead to $\sigma_d = 3.8 \pm 0.2$ and $\sigma_p = 1.3 \pm 0.1$, in disagreement with the values measured experimentally.

of depinning and pinning clusters as a function of the threshold C. They show the following behaviors

$$\begin{aligned} N_d &\sim C^{\chi_d} \quad \text{with} \quad \chi_d \simeq 1.7 \pm 0.2 \\ N_p &\sim C^{\chi_p} \sim N_0 \quad \text{with} \quad \chi_p \simeq 0 \end{aligned} \tag{13}$$

We compute then the total area covered by the depinning and pinning clusters as a function of the threshold C. As shown in Fig. 8, they vary as

$$\begin{aligned} A_d &\sim -\log(C) \\ A_p &\sim C^{-\kappa_p} \quad \text{with} \quad \kappa_p = 0.42 \pm 0.03 \end{aligned} \tag{14}$$

The logarithmic variations of A_d with C indicates an exponent value $\kappa_d = 0$ if one seeks to characterize the scaling relation $A_d \sim C^{-\kappa_d}$. The ratio of the area covered by the clusters over their total number gives the average cluster size

$$\langle S_d \rangle = N_d/A_d \quad \text{and} \quad \langle S_p \rangle = N_p/A_p. \tag{15}$$

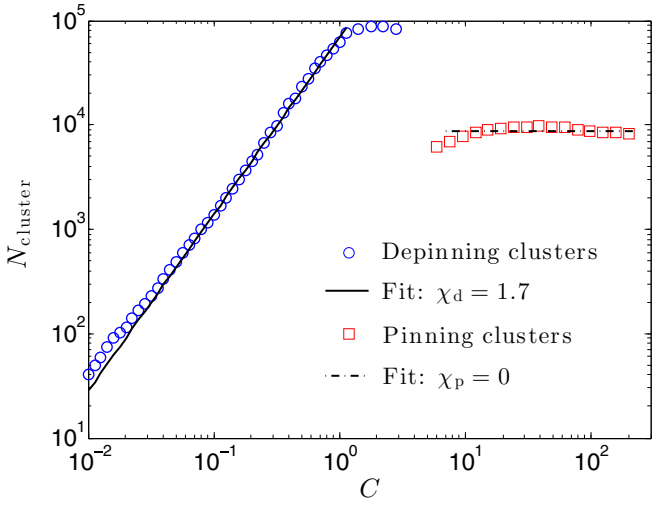

FIG. 7. Variations of the number of depinning and pinning clusters with the threshold C.

The latter can be related to the threshold C from the integrals $\langle S_{\rm d}\rangle = \int_0^\infty S_{\rm d}\, P(S_{\rm d})\, dS_{\rm d}$ and $\langle S_{\rm p}\rangle = \int_0^\infty S_{\rm p}\, P(S_{\rm p})\, dS_{\rm p}$ of the cluster size distributions of Eq. (12). This gives the following scaling relations

$$\begin{aligned} \langle S_{\rm d}\rangle &= (S_{\rm d}^\star)^{2-\gamma_{\rm d}} \sim C^{-\sigma_{\rm d}(2-\gamma_{\rm d})} \\ \langle S_{\rm p}\rangle &= (S_{\rm p}^\star)^{2-\gamma_{\rm p}} \sim C^{-\sigma_{\rm p}(2-\gamma_{\rm p})} \end{aligned} \tag{16}$$

We can now introduce the scaling laws (13), (14), and (16) in Eq. (15) to relate these exponents together through

$$\begin{aligned} \kappa_{\rm d} &= \sigma_{\rm d}(2-\gamma_{\rm d}) - \chi_{\rm d} \\ \kappa_{\rm p} &= \sigma_{\rm p}(2-\gamma_{\rm p}) - \chi_{\rm p} \end{aligned} \tag{17}$$

These expressions simplify to

$$\begin{aligned} \sigma_{\rm d} &= \chi_{\rm d}/(2-\gamma_{\rm d}) \\ \sigma_{\rm p} &= \kappa_{\rm p}/(2-\gamma_{\rm p}) \end{aligned} \tag{18}$$

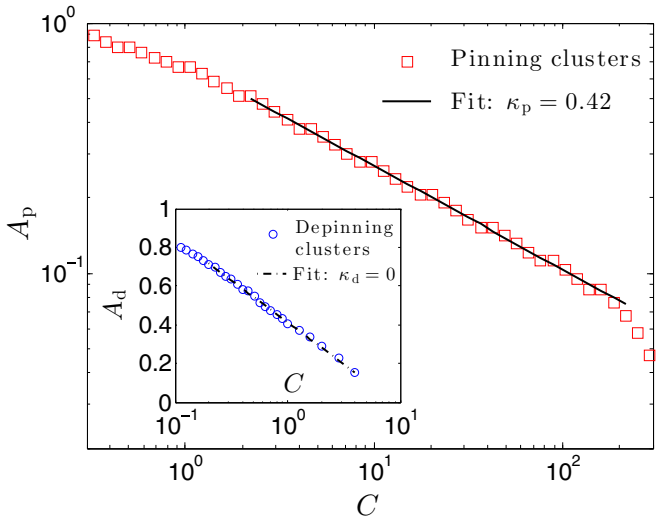

FIG. 8. Area covered by the pinning and the depinning clusters on the activity maps of Fig. 5 normalized by the total area crossed by the crack.

after taking into account that both $\kappa_{\rm d}$ and $\chi_{\rm p}$ are equal to zero. These last relations provide independent estimates of the exponents $\sigma_{\rm d} \simeq 3.8$ and $\sigma_{\rm p} \simeq 1.2$ that are in good agreement with their estimation made in Fig. 6 from the collapse of the cluster size distributions computed at different threshold values. And at the same time, it confirms the gap between the numerically determined and experimentally measured value of both exponents.

Before getting to the origin of this discrepancy, we provide some insights on the physical meaning of the exponent $\sigma_{\rm d}$ and a possible interpretation of its value as measured in our simulations. Consider the size $S_{\rm av}^*$ of the largest avalanches as we drive the crack at finite but small velocity $v_{\rm m}$. It follows $S_{\rm av}^* \sim \xi^{1+\zeta}$ where ξ is the correlation length along the crack line. Since the correlation length diverges as $\xi \sim v_{\rm m}^{-\nu/\theta}$ when the driving velocity vanishes, the typical size of the largest avalanches diverges too, following the scaling behavior $S_{\rm av}^\star \sim v_{\rm m}^{-\sigma_{\rm d}^{\rm av}} \sim v_{\rm m}^{-(1+\zeta)\,\nu/\theta}$. From the relations between critical exponents already used in Sec. III B, one obtains $\sigma_{\rm r}^{\rm av} = (1/\zeta + 1)/(1/\beta - 1)$ that simplifies to $\sigma_{\rm d}^{\rm av} = 1 + 1/\zeta \simeq 3.58 \pm 0.02$ after using $\beta = 1/2$ determined previously and the value of the roughness exponent $\zeta \simeq 0.388$ [57]. This value is surprisingly close of the exponent $\sigma_{\rm d} \simeq 3.8$ that characterizes the variations of cut-off cluster size when the velocity matrix is thresholded at different levels $C\, v_{\rm m}$.

This observation calls for the following comment: in our analysis, we considered a fixed velocity $v_{\rm m}$ of the front, and characterized the distribution of depinning clusters defined from the regions where the local velocity was larger than $v_{\rm thres} = C\, v_{\rm m}$. We observed that the smaller the threshold, the larger the size of the depinning clusters, and we could evidence the following scaling $S_{\rm d}^\star \sim v_{\rm thres}^{-\sigma_{\rm d}}$. We believe that this procedure reveals the depinning clusters as they would be observed if the driving velocity was actually equal to $v_{\rm thres}$. From this postulate, $\sigma_{\rm d}$ and $\sigma_{\rm d}^{\rm av}$ are then the very same exponent as they both characterize the divergence of the size of the largest depinning cluster or avalanche when the driving velocity goes to zero. Note that we need to assume here that the largest avalanche size $S_{\rm av}^*$ is proportional to the largest cluster size $S_{\rm d}^*$. This was indeed observed by Laurson *et al.* [31] who found $S_{\rm d} \sim S_{\rm av}$ for the largest events. Overall, our result suggests an interesting method for the analysis of depinning transition: scaling relations depicting the divergence of quantities of interest with the distance to the critical point can be determined without performing several experiments or simulations at different driving velocities. Indeed, they can be achieved from a single study performed at some fixed velocity $v_{\rm m}$ through the thresholding of the obtained velocity field at different levels $v_{\rm thres} = C\, v_{\rm m}$ and the scaling behavior in terms of $v_{\rm thres}$.

D. Distribution of crack velocities

We now move to the study of the distribution $p(v)$ of local crack speeds. We consider the velocity values stored in the velocity matrix V and compute their probability density function that is shown in Fig. 9. It shows two scaling regimes

$$\begin{aligned} v \gtrsim v_{\rm m} &\Rightarrow p(v) \sim v^{-(\eta_{\rm d}-1)} \quad \text{with} \quad \eta_{\rm d} = 2.0 \pm 0.1 \\ v \ll v_{\rm m} &\Rightarrow p(v) \sim v^{-(\eta_{\rm p}-1)} \quad \text{with} \quad \eta_{\rm p} = 1.6 \pm 0.1 \end{aligned} \tag{19}$$

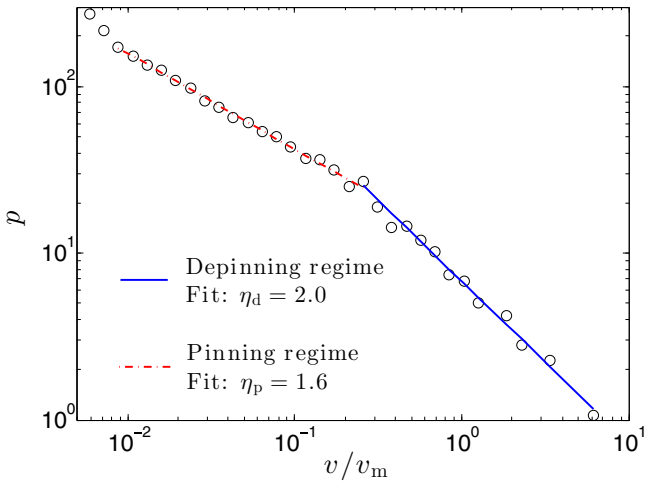

FIG. 9. Distribution of local crack velocity as measured from the waiting time matrix. The power-law fit of the pinning ($v \ll v_m$) and depinning ($v \gtrsim v_m$) regime using Eq. (19) provides the value of the velocity distribution exponents $\eta_p = 1.6$ and $\eta_p = 2.0$.

Large velocities $v > v_m$ correspond to the depinning domains while lower speeds $v < v_m$ correspond to the pinned regions. To confirm the value of these exponents, we follow Tallakstad *et al.* [24] and relate $p(v)$ with the area covered by the clusters using $A_d = \int_{Cv_m}^{v_{max}} p(v)dv \sim -\log(C)$ and $A_p = \int_0^{v_m/C} p(v)dv \sim C^{-\kappa_p}$ [see Eq. (14)]. This gives

$$\begin{aligned} \eta_d &= 2 + \kappa_d = 2 \\ \eta_p &= 2 - \kappa_p \simeq 1.58 \pm 0.03 \end{aligned} \tag{20}$$

which are well satisfied using the values of $\kappa_d = 0$ and $\kappa_p \simeq 0.42$ determined in Fig. 8.

How does the velocity distribution predicted by the depinning model compare to the experimental one? For the analysis of their experimental data, Mäløy *et al.* [7] considered the velocity $v_{front}(z,t)$ along the front that they inferred from the values of the velocity matrix using the procedure described in Ref. [7]. Sampling over different times t and locations z, they obtained the velocity distribution $P(v_{front})$ that relates to the distribution computed directly from the velocity matrix through the relation $p(v) = P(v)\, v/v_m$ [24]. The depinning regime $v_{front} > v_m$ was shown to display a remarkably robust behavior $P(v_{front}) \sim v_{front}^{-\eta_d^{exp}}$ that corresponds to $p(v) \sim v^{-(\eta_d^{exp}-1)}$ with an exponent $\eta_d^{exp} = 2.55 \pm 0.15$ that differs significantly from our theoretical prediction $\eta_d = 2$.

We would like now to show that the abnormally large exponent $\eta_d^{exp} > 2$ observed in the experiments is actually related to the other disagreement between theory and experiments reported in this study that concerns the exponential cutoff $S_d^\star \sim C^{-\sigma_d}$ of the cluster size distribution (see Sec. III C). Using the scaling relations (17) and (20) together gives

$$\eta_d = 2 + \sigma_d(2 - \gamma_d) - \chi_d, \tag{21}$$

which relates the velocity distribution through η_d with the cluster size distribution through σ_d and γ_d. This relation is verified both for experiments and in our simulations, however with different exponent values. With the exception of the size distribution exponent $\sigma_d \simeq \sigma_d^{exp} \simeq 1.55$, the other exponents show indeed significant differences as summarized in Table II. We believe that the mismatch between these exponents results from the basic crack growth mechanism assumed in our model that is different from the one involved in the experiments.

IV. DISCUSSION

How do we interpret the discrepancy between theory and experiment? We focus on the velocity distribution, and propose first a physical interpretation of the scaling $p(v) \sim v^{-\eta_d}$ with $\eta_d = 2$ observed in the simulations. We will see later that it sheds light on the abnormally large exponent $\eta_d^{exp} \simeq 2.55$ observed experimentally. We start from a simple situation and consider the evolution of a crack as it recovers a straight configuration after depinning from a single obstacle. As we are interested by the front evolution after having passed the obstacle, one can consider a homogenous medium and so achieve an exact solution [43]. The front geometry prior to depinning follows

$$\begin{aligned} c(z,t<0) = \frac{C\,d}{\pi}\Big[&\Big(1+\frac{z}{d}\Big)\ln\Big|1+\frac{z}{d}\Big| \\ &+\Big(1-\frac{z}{d}\Big)\ln\Big|1-\frac{z}{d}\Big|\Big], \end{aligned} \tag{22}$$

which corresponds to the equilibrium configuration of a crack trapped by an isolated obstacle of width $2d$ and strength $C = (G_c^O - \langle G_c\rangle)/\langle G_c\rangle$ where $G_c^O > \langle G_c\rangle$ is the toughness of the obstacle [63,64]. Using Eq. (22) as initial condition, the resolution of the evolution equation (6) with a homogeneous toughness field $\eta_c = 0$ gives the velocity field [43]

$$\begin{aligned} \frac{\partial c}{\partial t} = v_m + Cv_0\Big\{1 - \frac{1}{\pi}\Big[&\arctan\Big(\frac{v_0\,t}{d+z}\Big) \\ &- \arctan\Big(\frac{v_0\,t}{d-z}\Big)\Big]\Big\} \end{aligned} \tag{23}$$

TABLE II. Critical exponents measured numerically in both the depinning and pinning regime, and their comparison with the experimental values of Refs. [4,24].

Depinning	γ_d	σ_d	χ_d	κ_d	η_d
Sim.	1.55 ± 0.05	3.8 ± 0.2	1.7 ± 0.2	0	2.0 ± 0.1
Exp.	1.56 ± 0.04	1.77 ± 0.16	0.28	0.5	2.55 ± 0.15
Pinning	γ_p	σ_p	χ_p	κ_p	η_p
Sim.	1.65 ± 0.10	1.3 ± 0.1	0	0.42 ± 0.03	1.60 ± 0.05
Exp.	1.56 ± 0.04	2.81 ± 0.23	ø	ø	ø

valid in the central region of the front, $|z| < d$, and for small obstacles $d \ll \mathcal{L}$ compared to the structural length. Interestingly, it provides a simple interpretation of v_0 as the velocity jump $\frac{\partial c}{\partial t}(z,0) - v_m = C v_0$ at the onset of depinning. After a short transient $t \gg d/v_0$, Eq. (23) predicts a relaxation $\partial c/\partial t \simeq 2dC/(\pi t)$ that goes as the inverse of time. The same behavior holds also for the regions of the front further away from the obstacle, in $|z| > d$ [43]. We deduce from it the scaling of the velocity distribution $p(v) \sim 1/v^2$ during one avalanche resulting from the depinning of the front from a single obstacle. Depinning clusters observed during the evolution of the crack through disordered interfaces result from the depinning from several obstacles. However, our simulations show that the scaling of the velocity distribution remains unaffected and also follows $P(v) \sim 1/v^2$, irrespective of the cluster size and the number of obstacles involved in the depinning process (see Fig. 9). This provides interpretation for the statistics $P(v) \sim 1/v^2$ observed in our simulations in the depinning regime: It reflects the front relaxation between two pinned configurations.

This observation raises the question of the origin of the abnormally large exponent $\eta_d \simeq 2.5$ characterizing the depinning regime in the experiments. Insightful observations could be recently made using a discrete model of fracture that goes beyond brittle fracture and the assumptions made in our model. Gjerden *et al.* [53] investigated the propagation of a crack at a weak disordered interface between two elastic blocks connected by an array of parallel brittle fibers. When the force applied to one of the fiber exceeds its failure threshold, the fiber breaks and tensile forces are redistributed through the intact region of the interface assuming that blocks behave elastically. This redistribution mechanism produces cascades of failure events, qualitatively similar to the avalanche dynamics described in this study. For a weakly disordered interface, the simulation even recovers quantitatively the predictions of the depinning models and in particular the value of the roughness exponent $\zeta \simeq 0.4$ and the velocity distribution exponent $\eta_d \simeq 2.0$ [53,65]. But a more interesting regime takes place for strongly disordered interfaces. Indeed, the front dynamics is not governed anymore by the competition between the elasticity of the crack line and the disorder, but instead by the coalescence of the regions of broken fibers located ahead of the crack with the advancing crack itself. This transition from a brittle mechanism of crack growth to a quasibrittle one reflects on the scaling of the velocity distribution that follows $P(v) \simeq v^{-\eta_d}$ with $\eta_d \simeq 2.5$ [65,66]. This good agreement with the experimental observations suggests that crack growth between Plexiglas plates in Ref. [7]'s experiments is governed at small scales by the process of damage coalescence schematized in Fig. 10.

The existence of two distinct scaling regimes with exponent $\eta_d \simeq 2.0$ for brittle failure and $\eta_d \simeq 2.5$ for quasibrittle crack growth invites to discuss other experimental observations like the one of Barès *et al.* [67]. They investigated the fluctuations of the macroscopic crack speed $\langle v(t) \rangle = \langle v(z,t) \rangle_z$, measured at the scale of the specimen, and also observed a scaling behavior $p(\langle v \rangle) \sim \langle v \rangle^{-\eta_d^{\exp}}$ with $\eta_d^{\exp} \simeq 2.5$ in the depinning regime $\langle v \rangle > v_m$. As the scaling of the velocity distribution was shown to survive to upscaling [24], it is natural to interpret this behavior in terms of microscopic failure mechanism, and conjecture that microcracking does take place at small scales in the sintered materials used in Ref. [67]'s experiments.

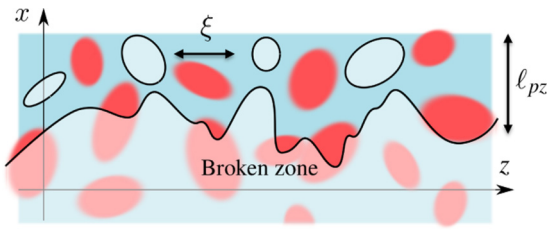

FIG. 10. Schematic representation of the damage coalescence process that takes place during failure of heterogeneous materials when the process zone size ℓ_{pz} is larger than the heterogeneity size ξ. In that regime, various statistical features of the front evolution are set by the process of damage coalescence, and do not agree with the predictions of the depinning model that describes brittle crack growth.

However, many questions remain open. First, we have mainly focused on the depinning regime, and proposed an interpretation for the scaling behavior of the velocity distribution in terms of local crack growth mechanism. What about the pinning regime? The observation of a scaling behavior with an exponent $\eta_p^{\exp} \simeq 1.4$ in Ref. [67]'s experiment, close to the theoretical prediction $\eta_p \simeq 1.6$ derived here in Fig. 9 is indication that the depinning model might be relevant for brittle, but also for quasibrittle crack growth. However, it does not capture the value of the exponent σ_p that describes the variations of the largest pinning clusters with the threshold velocity (see Sec. III C). Second, the geometry of the clusters and in particular their aspect ratio that displays a scaling behavior $\ell_x \sim \ell^{H^{\exp}}$ with an abnormally large exponent $H^{\exp} \simeq 0.6 > \zeta$ [24] remains still unexplained. These points should certainly deserve further investigations.

To conclude, we showed that the model of brittle fracture proposed in this study that builds on the concept of depinning transition can be used as a an efficient tool to predict crack evolution in disordered materials. Its success is conditioned to the implementation of two system specific characteristics, namely (i) the actual fracture properties of the material through the characteristic velocity v_0 and (ii) the specimen geometry through the structural length $\mathcal{L}$. However, the few but significant mismatches with some experimental observations suggest that an ingredient might be missing in the theoretical approach proposed in this work. We proposed that it relates to the mechanism of damage coalescence that takes place at small scales within the process zone in some materials. Back and forth between experiment and theory will certainly help to better characterize this mechanism and ultimately integrate it into the crack evolution equation proposed in this study.

ACKNOWLEDGMENTS

The authors would like to thank Daniel Bonamy, Pierre Le Doussal, Jean-Baptiste Lebond, and Alberto Rosso for enlightening discussions.

[1] S. Xia, L. Ponson, G. Ravichandran, and K. Bhattacharya, Phys. Rev. Lett. **108**, 196101 (2012).
[2] L. S. Dimas, G. H. Bratzel, I. Eylon, and M. Buehler, Adv. Func. Mat. **23**, 4629 (2013).
[3] A. Ghatak, Phys. Rev. E **89**, 032407 (2014).
[4] K. J. Måløy and J. Schmittbuhl, Phys. Rev. Lett. **87**, 105502 (2001).
[5] S. Santucci, L. Vanel, and S. Ciliberto, Phys. Rev. Lett. **93**, 095505 (2004).
[6] E. Bouchaud, G. Lapasset, and J. Planès, Europhys. Lett. **13**, 73 (1990).
[7] K. J. Måløy, A. Hansen, E. L. Hinrichsen, and S. Roux, Phys. Rev. Lett. **68**, 213 (1992).
[8] L. Ponson, D. Bonamy, and E. Bouchaud, Phys. Rev. Lett. **96**, 035506 (2006).
[9] D. Bonamy, S. Santucci, and L. Ponson, Phys. Rev. Lett. **101**, 045501 (2008).
[10] D. Bonamy, L. Ponson, S. Prades, E. Bouchaud, and C. Guillot, Phys. Rev. Lett. **97**, 135504 (2006).
[11] L. Ponson and D. Bonamy, Int. J. Frac. **162**, 21 (2010).
[12] S. Patinet, D. Vandembroucq, and S. Roux, Phys. Rev. Lett. **110**, 165507 (2013).
[13] V. Démery, A. Rosso, and L. Ponson, Europhys. Lett. **105**, 34003 (2014).
[14] E. Rolley and C. Guthmann, Phys. Rev. Lett. **98**, 166105 (2007).
[15] P. J. Metaxas, J. P. Jamet, A. Mougin, M. Cormier, J. Ferré, V. Baltz, B. Rodmacq, B. Dieny, and R. L. Stamps, Phys. Rev. Lett. **99**, 217208 (2007).
[16] S. Patinet, D. Bonamy, and L. Proville, Phys. Rev. B **84**, 174101 (2011).
[17] H. Herrmann and S. Roux, *Statistical Models for the Fracture of Disordered Media* (Elsevier, Amsterdam, 1990).
[18] J. Schmittbuhl, S. Roux, J. P. Vilotte, and K. J. Måløy, Phys. Rev. Lett. **74**, 1787 (1995).
[19] J. P. Bouchaud, E. Bouchaud, G. Lapasset, and J. Planès, Phys. Rev. Lett. **71**, 2240 (1993).
[20] L. Laurson, X. Illa, S. Santucci, K. T. Tallakstad, K. J. Måløy, and M. J. Alava, Nature Commun. **4**, 2927 (2013).
[21] S. Santucci, M. Grob, R. Toussaint, J. Schmittbuhl, A. Hansen, and K. J. Måløy, Europhys. Lett. **92**, 44001 (2010).
[22] J. Koivisto, J. Rosti, and M. J. Alava, Phys. Rev. Lett. **99**, 145504 (2007).
[23] L. Ponson, Phys. Rev. Lett. **103**, 055501 (2009).
[24] K. T. Tallakstad, R. Toussaint, S. Santucci, J. Schmittbuhl, and K. J. Måløy, Phys. Rev. E **83**, 046108 (2011).
[25] J. P. Sethna, K. A. Dahmen, and C. R. Myers, Nature (London) **410**, 242 (2001).
[26] A. Prevost, E. Rolley, and C. Guthmann, Phys. Rev. B **65**, 064517 (2002).
[27] F. F. Csikor, C. Motz, D. Weygand, M. Zaiser, and S. Zapperi, Science **318**, 251 (2007).
[28] J. Davidsen, S. Stanchits, and G. Dresen, Phys. Rev. Lett. **98**, 125502 (2007).
[29] A. Garcimartín, A. Guarino, L. Bellon, and S. Ciliberto, Phys. Rev. Lett. **79**, 3202 (1997).
[30] K. J. Måløy, S. Santucci, J. Schmittbuhl, and R. Toussaint, Phys. Rev. Lett. **96**, 045501 (2006).
[31] L. Laurson, S. Santucci, and S. Zapperi, Phys. Rev. E **81**, 046116 (2010).
[32] J. R. Rice, J. Appl. Mech. **52**, 571 (1985).
[33] H. Gao and J. R. Rice, J. Appl. Mech. **56**, 828 (1989).
[34] B. Lawn, *Fracture of Brittle Solids* (Cambridge University Press, Cambridge, 1993).
[35] A. Rosso, P. Le Doussal, and K. J. Wiese, Phys. Rev. B **80**, 144204 (2009).
[36] A. A. Middleton, P. Le Doussal, and K. J. Wiese, Phys. Rev. Lett. **98**, 155701 (2007).
[37] A. I. Larkin and Y. N. Ovchinnikov, *Nonequilibrium Superconductivity* (Elsevier, Amsterdam, 1989).
[38] A. Tanguy and T. Vettorel, Eur. Phys. J. B **38**, 71 (2004).
[39] S. Ramanathan, D. Ertas, and D. S. Fisher, Phys. Rev. Lett. **79**, 873 (1997).
[40] E. Katzav and M. Adda-Bedia, Europhys. Lett. **76**, 450 (2006).
[41] I. Kolvin, G. Cohen, and J. Fineberg, Phys. Rev. Lett. **114**, 175501 (2015).
[42] L. Ponson, Int. J. Frac. (to be published).
[43] J. Chopin, A. Bhaskar, and L. Ponson (unpublished).
[44] O. Lengliné, R. Toussaint, J. Schmittbuhl, J. E. Elkhoury, J. P. Ampuero, K. T. Tallakstad, S. Santucci, and K. J. Måløy, Phys. Rev. E **84**, 036104 (2011).
[45] M. Kardar, Phys. Reports **301**, 85 (1998).
[46] D. Ertas and M. Kardar, Phys. Rev. E **49**, R2532 (1994).
[47] O. Narayan and D. S. Fisher, Phys. Rev. B **48**, 7030 (1993).
[48] H. Leschhorn, T. Nattermann, S. Stepanow, and L. H. Tang, Ann. Phys. (N.Y.) **509**, 1 (1997).
[49] O. Duemmer and W. Krauth, J. Stat. Mech. (2007) P01019.
[50] D. Bonamy and E. Bouchaud, Phys. Rep. **498**, 1 (2011).
[51] D. Bonamy, J. Phys. D: Appl. Phys. **42**, 214014 (2009).
[52] K. Wiese and P. Le Doussal, in *Markov Processes and Related Fields* (Polymath, Moscow, 2007), Vol. 13, pp. 777–818.
[53] K. S. Gjerden, A. Stormo, and A. Hansen, Phys. Rev. Lett. **111**, 135502 (2013).
[54] D. Ertas and M. Kardar, Phys. Rev. Lett. **69**, 929 (1992).
[55] P. Chauve, P. Le Doussal, and K. J. Wiese, Phys. Rev. Lett. **86**, 1785 (2001).
[56] A. Tanguy, M. Gounelle, and S. Roux, Phys. Rev. E **58**, 1577 (1998).
[57] A. Rosso and W. Krauth, Phys. Rev. Lett. **87**, 187002 (2001).
[58] A. L. Barabási and H. E. Stanley, *Fractal Concepts in Surface Growth* (Cambridge University Press, Cambridge, 1995).
[59] M. Kardar, G. Parisi, and Y.-C. Zhang, Phys. Rev. Lett. **56**, 889 (1986).
[60] T. Nattermann, S. Stepanow, S. Tang, and H. Leschhorn, J. Phys. II **2**, 1483 (1992).
[61] O. Duemmer and W. Krauth, Phys. Rev. E **71**, 061601 (2005).
[62] J. Lin, E. Lerner, A. Rosso, and M. Wyart, Proc. Nat. Acad. Sci. **111**, 14382 (2014).
[63] J. Chopin, A. Prevost, A. Boudaoud, and M. Adda-Bedia, Phys. Rev. Lett. **107**, 144301 (2011).
[64] M. Vasoya, J.-B. Leblond, and L. Ponson, Int. J. Solids Struct. **50**, 371 (2013).
[65] A. Stormo, O. Lengliné, J. Schmittbuhl, and A. Hansen, Front. Phys. **4**, 18 (2016).
[66] K. G. Gjerden, A. Stormo, and A. Hansen, Front. Phys. **2**, 66 (2014).
[67] J. Barés, L. Barbier, and D. Bonamy, Phys. Rev. Lett. **111**, 054301 (2013).